CHALMERS
UNIVERSITY OF TECHNOLOGY

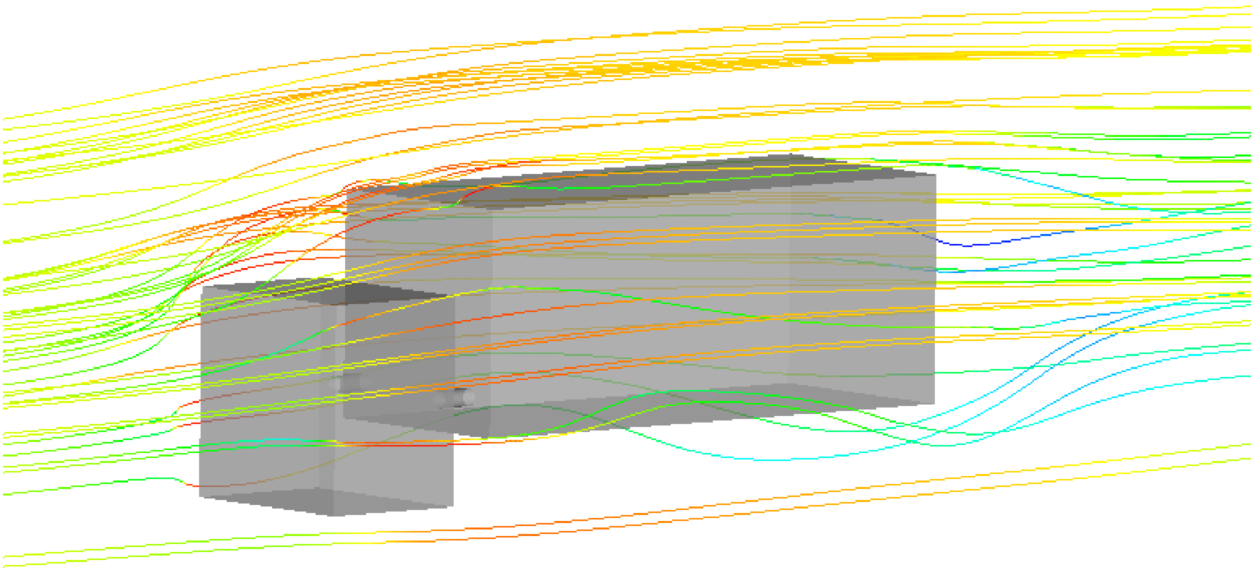

Accurate Prediction of the Flow Around a Truck and the Asymmetry of a Notch-back Ahmed Body

using Partially Averaged Navier-Stokes

Master's thesis in Applied Mechanics

Joacim Mattsson

Department of Applied Mechanics
CHALMERS UNIVERSITY OF TECHNOLOGY
Gothenburg, Sweden 2016

Master's thesis in applied mechanics 2016:69

Accurate Prediction of the Flow Around a Truck and the Asymmetry of a Notchback Ahmed Body

using Partially Averaged Navier-Stokes

JOACIM MATTSSON

CHALMERS
UNIVERSITY OF TECHNOLOGY

Department of Applied Mechanics
Division of Fluid Dynamics
Chalmers University of Technology
Gothenburg, Sweden 2016

Accurate Prediction of the Flow Around a Truck and the Asymmetry of a Notchback Ahmed Body
using Partially Averaged Navier-Stokes
JOACIM MATTSSON

Supervisor and examiner: Siniša Krajnović, Department of Applied Mechanics

Master's Thesis 2016:69
Department of Applied Mechanics
Division of Fluid Dynamics
Chalmers University of Technology
SE-412 96 Gothenburg
Sweden
Telephone: +46 31 772 1000

Cover: Generic truck with streamlines colored by velocity.

Gothenburg, Sweden 2016

Accurate Prediction of the Flow Around a Truck
using Partially Averaged Navier-Stokes
JOACIM MATTSSON
Department of Applied Mechanics
Division of Fluid Mechanics
Chalmers University of Technology

Abstract

Partially Averaged Navier Stokes is a turbulence model purported to seamlessly shift between RANS and LES solution to achieve an accurate solution in a cost effective manner. The simulations were carried out in the commercial software AVL FIRE. The purpose of this thesis was to show that PANS can be used to achieve results in good comparison to the references.

The flow around a generic truck, consisting of to boxes connected by two cylinders, was simulated at a Reynolds number of 510 000 based on the height of the trailer of the truck, using Partially Averaged Navier Stokes. The simulated flow turned steady after some simulated physical time. This was not expected to happen for such a blunt body, neither did it happen in the reference Large Eddy Simulation of the same body. Different numerical schemes, sizes of meshes, boundary conditions, and even workstations were used but all configuration gave these perplexing results.

Also the flow around a fully detailed half scale truck from VOLVO AB in a wind tunnel were meant to be simulated at a Reynolds number of $4.5 \cdot 10^6$. However due to some computational difficulties no meaningful results could be found. These difficulties included problems saving data files, which is theorized to be due to memory running out on the computational cluster.

Lastly a notchback Ahmed Body was simulated to try to reproduce the asymmetry of the wake that earlier has been seen in experiments. The flow was simulated at a Reynolds number of $1.9 \cdot 10^6$ based on the length of the body. No asymmetry of the flow was seen in the current work which contradicts the reference.

Keywords: CFD, PANS, Turbulence, Truck, Ahmed, Aerodynamics, VOLVO, AVL

Acknowledgments

I would like to thank my examiner and supervisor Professor Sinisa Krajnovic for help and support throughout the project. A big thank you also to Ph.D student Guglielmo Minelli for introducing me to the various software that was used, as well as being a valuable support for discussing issues and problems. Thank you also to my fellow Master Thesis Students in the research group who have been of great help.

A big thanks to AVL for providing the AVL Fire license and for the financing of the project. A special thank you to Chief CFD Developer at AVL, Branislav Basara, for expert assistance regarding the solver, and also to Jan Viher at AVL Slovenia, for extensive help with the meshing of the detailed truck.

Thank you to AB Volvo and especially Zenitha Chronéer from AB Volvo for providing the mesh for the fully detailed truck.

Nomenclature

Initialisms

CFD Computational Fluid Dynamics

CFL Courant-Friedrich-Lewy

DES Detached Eddy Simulation

DNS Direct Numerical Simulation

LES Large Eddy Simulation

PANS Partially-Averaged Navier-Stokes

PITM Partiallly Integrated Transport Model

RANS Reynolds Averaged Navier-Stokes

SFS Sub-Filter Scale

VR Variable Resolution

Greek Symbols

$\boldsymbol{\delta}_{ij}$ Kronecker delta

$\boldsymbol{\varepsilon}$ Turbulence dissipation rate $[m^2/s^3]$

$\boldsymbol{\zeta}$ Velocity scale ratio $[-]$

$\boldsymbol{\Lambda}$ Taylor length scale

$\boldsymbol{\nu}$ Kinematic Viscosity $[m^2/s]$

$\boldsymbol{\nu}_u$ Eddy Viscosity $[m^2/s]$

$\boldsymbol{\rho}$ Density $[kg/m^3]$

$\boldsymbol{\sigma}$ Model coefficient

$\boldsymbol{\mu}$ Dynamic Viscosity $[kg/(m \cdot s)]$

$\boldsymbol{\tau}$ Shear stress

$\boldsymbol{\tau}(\cdot,\cdot)$ Generalized second moment

Roman Symbols

$\boldsymbol{C, c}$ Model coefficients

$\boldsymbol{f}_\varepsilon$ Unresolved-to-total-dissipation-rate-ratio

$\boldsymbol{f}_k$ Unresolved-to-total-kinetic-energy-ratio

$\boldsymbol{k}$ Turbulence kinetic energy $[m^2/s^2]$

$\boldsymbol{p}$ Pressure $[N/m^2]$

$\boldsymbol{P}$ Production of k

$\boldsymbol{Re}$ Reynolds Number

$\boldsymbol{t}$ Time $[s]$

$\boldsymbol{u}$ Subfilter velocity component $[m/s]$

$\boldsymbol{U}$ Filtered velocity compontent $[m/s]$

$\boldsymbol{U}_\infty$ Mean velocity $[m/s]$

$\boldsymbol{u'}$ Root-mean-square of velocity fluctuation $[m/s]$

$\boldsymbol{V}$ Instantaneous velocity compontent $[m/s]$

Subscripts

$\boldsymbol{u}$ Unresolved quantity

Contents

1 Introduction

One of the most important factors when it comes to fuel efficiency of heavy vehicles, such as trucks, is the aerodynamic performance. Methods to analyze the aerodynamics of such vehicles includes wind tunnel testing and Computational Fluid Dynamics (CFD). Historically wind tunnel testing has been the main tool for aerodynamics analysis in the automotive industry. However, with growing processing capabilities the use of CFD is growing but primarily as a complement rather than a replacement, according to Kobayashi and Tsubokura [1].

Throughout the thesis the combination of a tractor and a trailer will be referred to simply as a truck. A truck, as well as an Ahmed body, is to be considered a bluff body and the flow field around such a body has the characteristics of being turbulent, highly three-dimensional, and unsteady, with areas of separation. Keeping these characteristics in mind is key to accurately and efficiently predict the flow field around any body using CFD.

For turbulent flows there are in general two prevailing approaches in CFD to solve the *Navier-Stokes* equations, namely Reynolds Averaged Navier-Stokes (RANS) and Large Eddy Simulation (LES). However with RANS being cheap but not very accurate and LES being expensive but accurate, there seems to be an opening for a method that combines the favourable features of these two methods.

1.1 Background

In RANS, the turbulence is modeled by some closure model, where the $k-\epsilon$-method is the most widespread. The flow around an operating truck is inherently unsteady, and with RANS being a steady method, it is clear that these models will fail to accurately predict the flow field. In addition to this, RANS is not well-suited to handle the regions of separation that are to be expected. However, the method is still used in the vehicle aerodynamics industry, as it can predict the drag coefficient C_D reasonably well.

In LES all scales that the grid permits are resolved and only the sub-grid scales are modeled. For this method to be accurate extremely high resolution is needed at the walls. For a case like an operating truck, with complex geometry and high Reynolds number, this would require mesh sizes and time steps not feasible with today's computing abilities.

The idea of a compromise between the computationally cheap, but inaccurate, RANS and the computationally expensive, but accurate, LES was first suggested by Speziale [2]. This idea is here referred to as Variable Resolution (VR). Two distinct paths has since been followed based on the VR idea. The bridging approach by Speziale [2], where a transition between LES and RANS occurs seamlessly, and the zonal approach by Spalart et al. [3], where the transition occurs at a specified cutoff length from the wall. The Detached Eddy Simulation (DES) by Spalart et al. [3] can be considered as the most widely adopted VR method in industry, and represents the zonal approach. In the bridging approach the two prevailing models are Partiallly Integrated Transport Model (PITM), suggested by Chaouat and Schiestel [4], and Partially-Averaged Navier-Stokes (PANS) originally suggested by Girimaji, Srinivasan, and Jeong [5]. The original PANS has been further improved by Basara et al. [6], in terms of the near-wall behaviour.

The PANS model has been investigated in several canonical problems with satisfactory results, including flow around a square cylinder, by Song and Park [7], and flow around Ahmed bodies, by Mirzaei, Krajnović, and Basara [8]. However for an industrial application such as the flow field around a truck it remains untested.

Östh and Krajnović [9] used LES to model the flow around a generic truck, consisting of two boxes connected by two cylinders. Different configurations of the truck were run at a Reynolds number, based on the width of the truck, of 510 000 and drag coefficients, pressure coefficients as well as flow structures were presented. This paper will be the basis of much of the work that will be presented in this thesis.

Also part of the works in Sims-Williams, Marwood, and Sprot [10], where asymmetric wakes for notchback Ahmed bodies has been studied will be referenced frequently. One of the bodies here will be simulated using PANS.

1.2 Aim

The aim of this thesis is to use PANS to reproduce the results for the analysis using LES of a generic truck in Östh and Krajnović [9]. Since LES is a well established model this will contribute to lend credibility to PANS as a model well suited for bluff bodies at reasonably high Reynolds numbers.

Further it also aims to investigate if the model can be used for a real industrial application and that computations can be performed in an acceptable time span for the industry. This will be done by performing a PANS analysis on a fully detailed half-scale VOLVO truck.

It also aims to reproduce the experimental results of the asymmetry of a notchback Ahmed body as presented in Sims-Williams, Marwood, and Sprot [10].

1.3 Outline

First some general theory about PANS as well as complementary material relevant for this project will be presented. Following this the three main parts of the thesis; the generic truck and the detailed truck, as well as the notchback Ahmed body, will be presented separately. These parts will include how the cases were set up as well as the obtained results and discussion of said results. Lastly conclusions will be drawn and suggestions for future works will be given.

2 Theory

Brief descriptions of the modeling equations and constants used in the PANS method will be presented here. For more detailed derivations the reader is referred to the references provided troughout the chapter. Further some additional quantities and equations used in the thesis will be defined and explained for reference.

2.1 PANS formulation

The following derivations are taken from Girimaji [11]. The derivation of the PANS equation starts from the instantaneous incompressible *Navier-Stokes* equations. Here in tensor notation

$$\begin{aligned} \frac{\partial V_i}{\partial t} + V_j \frac{\partial V_i}{\partial x_j} &= -\frac{1}{\rho}\frac{\partial p}{\partial x_i} + \nu \frac{\partial^2 V_i}{\partial x_i \partial x_i} \\ -\frac{\partial^2 p}{\partial x_i \partial x_i} &= \frac{\partial V_i}{\partial x_j}\frac{\partial V_j}{\partial x_i} \end{aligned} \tag{1}$$

The instantaneous velocity V_i can be decomposed using an arbitrary filter into a resolved field; U_i, and an unresolved field, u_i

$$V_i = U_i + u_i \tag{2}$$

Assuming that the filter is commutative with regards to the spatio-temporal operator, applying this filter to eq. (1) gives the PANS equations

$$\begin{aligned} \frac{\partial U_i}{\partial t} + U_j \frac{\partial U_i}{\partial x_j} + \frac{\partial \tau(V_i, V_j)}{\partial x_j} &= -\frac{1}{\rho}\frac{\partial p_u}{\partial x_i} + \nu \frac{\partial^2 U_i}{\partial x_i \partial x_i} \\ -\frac{\partial^2 p_u}{\partial x_i \partial x_i} &= \frac{\partial U_i}{\partial x_j}\frac{\partial U_j}{\partial x_i} + \frac{\partial^2 \tau(V_i, V_j)}{\partial x_i \partial x_j} \end{aligned} \tag{3}$$

Where the lower case u subscript refers to an uresolved quantity. The term $\tau(V_i, V_j)$ gives the effect of the unresolved field upon the resolved field, termed as Sub-Filter Scale (SFS) stress. $\tau(A, B)$ is the generalized second moment defined by Germano [12]

$$\tau(A, B) =< AB > - < A >< B > \tag{4}$$

Here an entity inside of angled brackets indicates that it has been filtered.

2.2 Modeling

The PANS equations, eq. (3), can not be solved explicitly but they need a closure model. The SFS stress is modelled using a *Boussinesq* constitutive model as

$$\tau(V_i, V_j) = -2\nu_u S_{ij} + \frac{2}{3} k_u \delta_{ij} \tag{5}$$

With the subscript lower case u referring to the unresolved quantity. The resolved stress tensor S_{ij} is expressed as

$$S_{ij} = \frac{1}{2}\left(\frac{\partial U_i}{\partial x_j} + \frac{\partial U_j}{\partial x_i}\right) \tag{6}$$

And the eddy viscosity ν_u as

$$\nu_u = C_\mu \frac{k_u^2}{\varepsilon_u} \tag{7}$$

The transport equations for the unresolved turbulent kinetic energy, k_u, and the unresolved dissipation, ε_u, are

$$\begin{aligned}
\frac{\partial k_u}{\partial t} + U_j \frac{\partial k_u}{\partial x_j} &= P_u - \varepsilon_u + \frac{\partial}{\partial x_j}\left(\frac{\nu_u}{\sigma_{k_u}} \frac{\partial k_u}{\partial x_j}\right) \\
\frac{\partial \varepsilon_u}{\partial t} + U_j \frac{\partial \varepsilon_u}{\partial x_j} &= C_{\varepsilon 1} P_u \frac{\varepsilon_u}{k_u} - C^*_{\varepsilon 2} \frac{\varepsilon_u^2}{k_u} + \frac{\partial}{\partial x_j}\left(\frac{\varepsilon_u}{\sigma_{\varepsilon_u}} \frac{\partial \varepsilon_u}{\partial x_j}\right)
\end{aligned} \tag{8}$$

Where the unresolved quantites; kinetic energy, k_u, disspation, ε_u, are defined as

$$\begin{aligned}
k_u &= \frac{1}{2}\tau(V_i, V_i) \\
\varepsilon_u &= \nu\tau\left(\frac{\partial V_i}{\partial x_j}, \frac{\partial V_j}{\partial x_i}\right)
\end{aligned} \tag{9}$$

The unresolved production term is

$$P_u = \tau(V_i, V_j) \frac{\partial U_i}{\partial x_j} \tag{10}$$

The model coefficients in this model are defined in Girimaji, Srinivasan, and Jeong [5] as: $C_{\varepsilon 1} = 1,44$, $C_{\varepsilon 2} = 1.92$, $\sigma_k = 1.0$, $\sigma_\varepsilon = 1.3$, and according to Girimaji and Abdol-Hamid [13]; $C_\mu = 0.09$ just as in the parent RANS model. Further:

$$C^*_{\varepsilon 2} = C_{\varepsilon 1} + \frac{f_k}{f_\varepsilon}(C_{\varepsilon 2} - C_{\varepsilon 1}); \qquad \sigma_{k_u} = \sigma_k \frac{f_k^2}{f_\varepsilon}; \qquad \sigma_{\varepsilon_u} = \sigma_\varepsilon \frac{f_k^2}{f_\varepsilon} \tag{11}$$

The unresolved-to-total-kinetic-energy-ratio, $f_k = \frac{k_u}{k}$, and unresolved-to-total-dissipation-ratio, $f_\varepsilon = \frac{\varepsilon_u}{\varepsilon}$, are the control parameters that control the filtering and thus essentially determines how much of the turbulence that is resolved and how much that is modeled. Here $0 \leqslant f_k \leqslant f_\varepsilon \leqslant 1$. If $f_k = 1$ it reduces to a RANS closure model where no turbulent scales are resolved. On the other hand, if $f_k = 0$, it acts as a DNS solution. These parameters were elaborated by Girimaji and Abdol-Hamid [13] to vary with grid size as

$$f_k(\mathbf{x}) = \frac{1}{\sqrt{C_\mu}} \left(\frac{\Delta}{\Lambda}\right)^{2/3} \tag{12}$$

With $\Lambda = k^{1.5}/\varepsilon$ being the Taylor scale, and $\Delta = \sqrt[3]{\Delta_x \times \Delta_y \times \Delta_z}$ the average cell dimension. Here it is assumed that $f_\varepsilon \approx 1$, based on eq. (12) being derived for high-Re flows with the dissipative scales assumed to be unresolved.

2.3 PANS $k - \varepsilon - \zeta - f$

As the PANS-model reduces to RANS in the limit of $f_k = 1$ it is clear that the PANS-model will only be as good as the RANS-model. Therefore as a mean to improve the near-wall behaviour of the PANS-model the parent RANS needs to be improved. This was done by Basara et al. [6] by applying the PANS methodology to a four equation model presented by Hanjalić, Popovac, and Hadžiabdić [14]. The two additional quantities solved for in this model are the unresolved velocity scale ratio $\zeta_u = \frac{\overline{v}_u^2}{k_u}$, with $\overline{v}$ being the velocity scale, and an elliptic relaxation function f_u. These integrations are purported to be an enhancement on the previously used two-equation closure models, especially in terms of near-wall behaviour. The equations for this model are given as

$$
\begin{aligned}
\nu_u &= C_\mu \zeta_\mu \frac{k_u^2}{\varepsilon_u} \\
\frac{\partial k_u}{\partial t} + U_j \frac{\partial k_u}{\partial x_j} &= P_u - \varepsilon_u + \frac{\partial}{\partial x_j}\left(\frac{\nu_u}{\sigma_{k_u}} \frac{\partial k_u}{\partial x_j}\right) \\
\frac{\partial \varepsilon_u}{\partial t} + U_j \frac{\partial \varepsilon_u}{\partial x_j} &= C_{\varepsilon 1} P_u \frac{\varepsilon_u}{k_u} - C^*_{\varepsilon 2} \frac{\varepsilon_u^2}{k_u} + \frac{\partial}{\partial x_j}\left(\frac{\varepsilon_u}{\sigma_{\varepsilon_u}} \frac{\partial \varepsilon_u}{\partial x_j}\right) \\
C^*_{\varepsilon 2} &= C_{\varepsilon 1} + f_k (C_{\varepsilon 2} - C_{\varepsilon 1}) \\
\frac{\partial \zeta_u}{\partial t} + U_j \frac{\partial \zeta_u}{\partial x_j} &= f_u - \frac{\zeta_u}{k_u} P_u + \frac{\zeta_u}{k_u} \varepsilon_u (1 - f_k) + \frac{\partial}{\partial x_j}\left(\frac{\nu_u}{\sigma_{\zeta_u}} \frac{\partial \zeta_u}{\partial x_j}\right) \\
L_u^2 \nabla^2 f_u - f_u &= \frac{1}{T_u}\left(C_1 + C_2 \frac{P_u}{\varepsilon_u}\right)\left(\zeta_u - \frac{2}{3}\right)
\end{aligned}
\tag{13}
$$

The coefficients C_μ, c_1, c_2, and $C_{\varepsilon 2}$ are 0.22, 0.4, 0.65, and 1.9 respectively. L_u is the length scale and is defined as

$$
L_u = C_L \cdot \max\left[\frac{k_u^{3/2}}{\varepsilon}, C_\eta \left(\frac{\nu^3}{\varepsilon}\right)^{1/4}\right] \tag{14}
$$

And the time scale T_u as

$$
T_u = \max\left[\frac{k_u}{\varepsilon}, C_\tau \left(\frac{\nu}{\varepsilon}\right)^{1/2}\right] \tag{15}
$$

The additional constants used for this model are $C_L = 0.36$ and $C_\tau = 6.0$.

Further this model is improved by adopting a compound wall treatment, as presented in Popovac and Hanjalic [15], which combines integration up to the wall with the classic *law of the wall* functions. The wall shear stress, production, and dissipation are blended as

$$
\phi = \phi_v e^{-\Gamma} + \phi_t e^{-1/\Gamma} \tag{16}
$$

With subscripts v and t indicates viscous and fully turbulent quantities respectively. Γ is a function of the non-dimensionalized wall-normal distance n^+ as

$$
\Gamma = \frac{0.01 (n^+)^4}{1 + 5 n^+} \tag{17}
$$

2.4 Turbulent quantities

In LES, the turbulence is numerically developed and only the dissipative scales modeled. In PANS however, also larger scales are modeled meaning turbulent quantities has to be prescribed at the inlet boundary. To give an estimate of these quantities, in form of kinetic energy and dissipation, to a boundary or initial condition of a flow the turbulence intensity is used. This is a measure of the ratio of the root-mean-square value of the velocity fluctuations, u', and the mean velocity of the flow, U_∞

$$I = \frac{u'}{U_\infty} \tag{18}$$

From the fluctuations the turbulence kinetic energy can be calculated

$$k = \frac{u'^2}{2} \tag{19}$$

The turbulence dissipation is calculated using the eddy viscosity as in eq. (13). Here the velocity scale is set to $\zeta = 2/3$ and for PANS, the eddy viscosity is typically set to be around $\nu_u = 0.4\nu$. Solving for the dissipation gives

$$\varepsilon = \frac{\zeta C_\mu k^2}{\nu_u} \tag{20}$$

2.5 Resolution

The spatial resolution of a numerical mesh is typically measured in viscous wall units which are nondimensionalized distances. These units are: the wall-normal wall unit, n^+ (often referred to as y^+), the streamwise unit s^+, and the unit parallel to the surface of the wall but normal to the streamwise direction, l^+. These are defined as

$$\begin{aligned} n^+ &= \frac{n \cdot u_\tau}{\nu} \\ s^+ &= \frac{s \cdot u_\tau}{\nu} \\ l^+ &= \frac{l \cdot u_\tau}{\nu} \end{aligned} \tag{21}$$

With n, s, and l, being the real dimensions of the respective distance and u_τ being the friction velocity.

$$u_\tau = \frac{\tau_w}{\rho} \tag{22}$$

Here τ_w is the shear stress at the wall.

For an LES-solution these units should typically be $n^+ < 1$, $s^+ < 100$, and $l^+ < 30$. For PANS however, part of the attraction is that the two latter of these units can be relaxed. Relaxing these will result in fewer number of cells in a mesh and will thus reduce computational time and effort.

When it comes to temporal resolution it is quantified by the Courant-Friedrich-Lewy (CFL) condition. The CFL number is defined as

$$CFL = \frac{V \cdot \Delta t}{\Delta x} \tag{23}$$

This can heuristically be said to be a measurement of how many cells a fluid particle passes for each time step. For an explicit time marching scheme this number must be lower than one. This must not necessarily be the case for implicit time marching schemes although it is generally desirable.

2.6 Numerical Schemes

Three different numerical schemes have been used to discretize the convective terms of the governing equations in this project, namely Central Difference, Minmod, and AVL Smart. On a uniform grid the value of a property, ϕ, on the face of two cells can be interpolated using a Central Difference Scheme as described in detail in Versteeg and Malalasekera [16]

$$\begin{aligned} \phi_w &= \frac{\phi_W + \phi_P}{2} \\ \phi_e &= \frac{\phi_P + \phi_E}{2} \end{aligned} \tag{24}$$

This scheme is second order accurate. However it comes at the cost of possible numerical problems such as spurious oscillations, when the flow is dominated by convection rather than diffusion. One way to come to terms to this is using so called Flux Limiter functions for high resolution schemes. These higher order schemes are based on the first order accurate upwind scheme, $\phi_e = \phi_P$, which is extended to a higher order scheme with the function $\Psi(r)$ as stated in Versteeg and Malalasekera [16]

$$\phi_e = \phi_P + \frac{1}{2}\Psi(r)(\phi_E - \phi_P) \tag{25}$$

Where r is the successive gradients of the cells

$$r = \frac{\phi_P - \phi_W}{\phi_E - \phi_P} \tag{26}$$

It can easily be seen that for $\Phi(r) = 1$ this scheme is identical to the central differencing scheme, and that $\Phi(r) = 0$ is identical to the upwind scheme. The functions Ψ is meant to limit the fluxes to physically sound values and is thus called flux limiter functions.

The Minmod flux limiter function is defined in Sweby [17] as

$$\Psi(r) = max\{0, min(1, r)\} \tag{27}$$

and AVL Smart is defined in AVL FIRE 2014 [18] as

$$\Psi(r) = max\{0, min(\beta_1 r, 0.5f(1 + f^*) + 0.5((1 - f^*)r, \beta_2\} \tag{28}$$

Where $\beta_1 = \beta_2 = 0.75$. f is an flow-oriented interpolation factor. For more detail on this the reader is refered to the documentation of AVL FIRE 2014 [18]. This variety of the SMART scheme is more diffusive but has better convergence properties than the original SMART.

For the time integration a second order accurate three time level scheme is used to evaluate the derivatives. This scheme is implicit and thus unconditionally stable. A constant time step is used and the time derivative is discretized as follows

$$\left(\frac{d\phi}{dt}\right)_n = \frac{3\phi^n - 4\phi^{n-1} + \phi^{n-2}}{2\Delta t} \tag{29}$$

2.7 Porous media

Porous regions can sometimes be used to simulate flow through regions with fine clearances for the the fluid to pass through. Flow through porous media at higher velocities results in a pressure loss due to both viscous and inertial losses. This loss can be modeled using the *Darcy-Forchheimer*-equation. Here α $[1/m^2]$ is the viscous loss constant. When discussing porous media ζ $[1/m]$ is the inertial loss constant and not the velocity scale ratio as in the rest of the thesis.

$$\frac{\partial p}{\partial x} = -\alpha \cdot \mu \cdot w - \zeta \cdot \frac{\rho}{2} \cdot w^2 \tag{30}$$

2.8 Computational Cluster

All simulations presented in this thesis are performed at the Triolith Cluster, located in Linköping, Sweden, at the Swedish National Infrastructure of Computing, SNIC. This cluster has 1524 *thin* computing nodes with 16 cores and 32 GB of memory for each core. It also has 56 *fat* computing nodes which has larger memory. These nodes also has 16 cores each but has 128 GB of memory. The cluster also has other nodes with other sizes of memory but these are not used in this project, nor will they be discussed.

3 Generic Truck

The geometry used for the generic truck is the same as the one that was used in Allan [19] as well as in Östh and Krajnović [9] and can be seen in fig. 1. The width of the trailer was set to $b = 0.305\ m$ in both of the references as well as in the current work. The cylinders in the LES had a diameter of $0.08b$ whereas in the experiments the diameter was $0.09b$. For the current work the smaller diameter of the LES was adopted since more data for comparison was available for this case. The centers of the cylinders were placed at half the height of the front box.

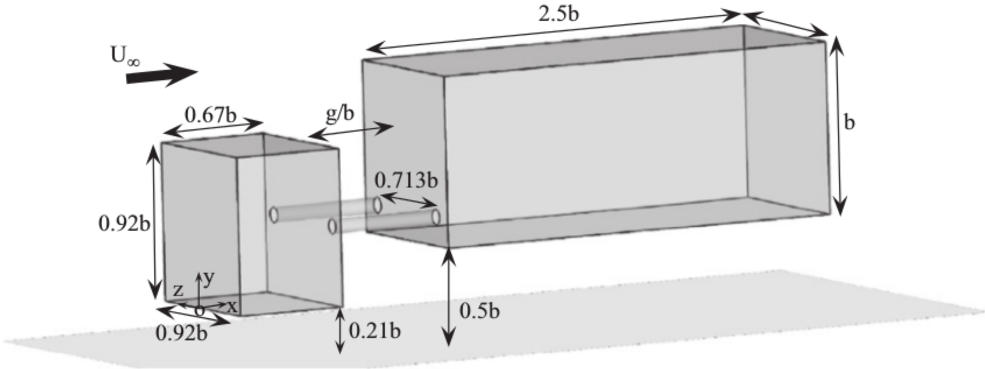

Figure 1: Simplified Truck (figure from Östh and Krajnović [9])

The Reynolds number, based on the width b of the trailer, was $Re_b = \frac{U_\infty b}{\nu} = 510\ 000$ and the mean velocity $U_\infty = 24.4\ m/s$. This led to a kinematic viscosity of $\nu = 1.4353 \cdot 10^{-5}\ m^2/s$

Four different configurations, referred to as cases, of this truck were presented in Östh and Krajnović [9]. Case 1 with sharp leading edges of the front box and gap-to-width ratio $g/b = 0.17$, Case 2 with rounded leading edges of the front box and $g/b = 0.17$, Case 3 with sharp leading edges of the front box and $g/b = 0.67$, and lastly, Case 4 with rounded leading edges of the front box and $g/b = 0.67$. Due to limitations in time and computing resources only one of these cases was studied in the current work, and that was Case 1. There was no further reason for this choice other than that this case required the smallest mesh. In fig. 2 a schematic illustration of the computational domain can be seen. Given the length of the domain and the mean velocity of the flow, one fluid particle passes the domain in $0.4088s$.

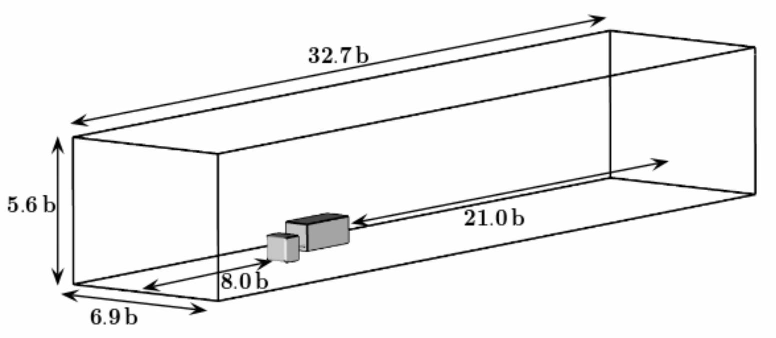

Figure 2: Computational Domain (figure from Östh and Krajnović [9])

The notation for the different faces of the truck follows what was established in Östh and Krajnović [9], here illustrated in fig. 3. In the first part of the notation FB indicates front box whereas RB indicates rear box. In the second part FF, TF, BF, GF, and LF stands for front face, top face, base face, ground face, and lateral face respectively.

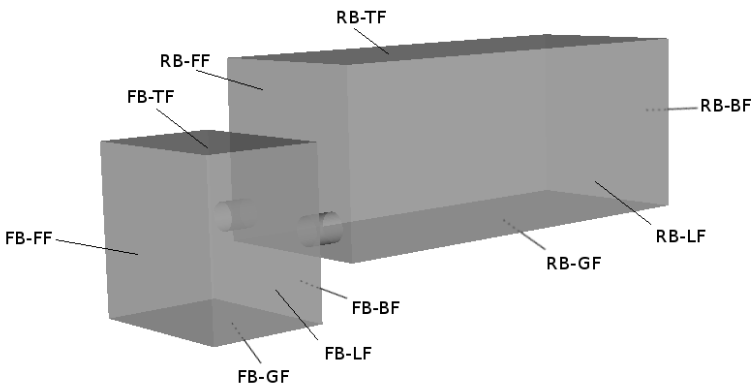

Figure 3: Notation of faces

The case was solved using the finite volume CFD code AVL FIRE 2014 [18], in which the PANS $k-\varepsilon-\zeta-f$-model is implemented.

3.1 Computational Mesh

In order to compare the results from the LES in Östh and Krajnović [9] and the PANS results of this thesis it would have been desirable to use the same mesh for both models. However the mesh from Östh and Krajnović [9] was not available and a new mesh had to be created. The hexagonal mesh was created using the commercial mesher ANSYS ICEM CFD 14.0 [20]. In order to maintain full control over all mesh parameters it was created manually as a structured mesh.

Around the truck an O-grid was created, which was split up further to fit the geometry of the truck. This included one O-grid around each of the connecting cylinders. In fig. 4 the blocking structure is visualized, with the lines being edges that separates the different blocks.

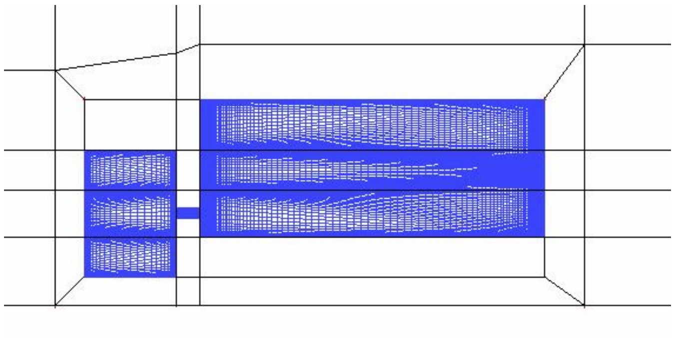

Figure 4: Blocking structure as seen from side of truck

Determining the spacing of the cells closest to the surface of truck was done using wall units as presented in section 2.5. A wall normal spacing for the first cell at the surface of the truck as $\Delta n = 0.00016b = 4.88 \cdot 10^{-5}\ m$ was used, in accordance with Östh and Krajnović [9]. Since the floor of the domain was moving to simulate a moving truck, no boundary layer would form on the floor and thus there was no need to resolve it. The boundary layers that would form on walls and ceiling are sufficiently far away from the body so these also did not need to be resolved.

The fine mesh that was used in Östh and Krajnović [9] consisted of $13.8 \cdot 10^6$ cells. Naturally PANS is only worthwhile if smaller meshes can be used. Thus a fine mesh consisting of about $13 \cdot 10^6$ cells was initially created. This mesh was then coarsened by increasing the spanwise and streamwise cell dimensions, and consequently the corresponding wall units, on the truck surface to a medium sized mesh with $6.55 \cdot 10^6$ cells. Also a small mesh of $3.86 \cdot 10^6$ was constructed by further coarsening the mesh.

The quality of the meshes was quantified using the *2x2x2 Determinant* function in ANSYS ICEM CFD 14.0 [20]. The determinant of the jacobian matrix of a cell is calculated at each corner of the cell. The smallest determinant divided by the largest then represents the mesh quality. A value of 1 thus represents a perfectly rectangular cell with this value decreasing with the quality of the cell. There is no well-defined limit of what values are acceptable but an aim has been to keep the quality at least around 0.6

The worst cell of the large mesh had a quality of 0.673 and over 99% of the cells had values over 0.8. Naturally, when reducing the number of cells, some cells will deteriorate, thus for the medium mesh the worst cell had a quality of 0.573 with more than 99% of the cells had values better than 0.75. The worst cell quality of the small mesh was 0.512 and more than 99% of the cells had a quality over 0.7.

3.2 Boundary and Initial Conditions

The boundary conditions for the case of the generic truck were chosen based on those used in Östh and Krajnović [9]. These were in turn chosen to mimic the conditions for the experimental case in Allan [19]. The inlet was set as a velocity inlet with uniform velocity at $U_\infty = 24.4\ m/s$. In neither the LES of Östh and Krajnović [9], nor the experiments of Allan [19], turbulence intensity was specified. Assuming a turbulence intensity of 0.5%, which is typical for wind tunnels, the turbulent kinetic energy was calculated from eq. (19) to $7.442 \cdot 10^{-3}\ m^2/s^2$. The dissipation rate was calculated with the eddy viscosity set to $\nu_u = 0.35\nu$, using eq. (20), to $1.61697\ m^2/s^3$. An alternative boundary condition for the turbulence was also tried. Here the turbulence kinetic energy was $1.38 \cdot 10^{-2}\ m^2/s^2$ and the dissipation $0.8\ m^2/s^3$. This corresponded to a eddy viscosity of about $\nu_u = 2.4\nu$.

For the outlet the homogeneous Neumann boundary condition was used. The walls, ceiling, and surface of the truck were all set as no-slip stationary walls. To mimic a truck driving on a road, the floor was set as a no-slip moving wall with the velocity being the same as the free-stream velocity of the flow, U_∞.

The initial velocity of the flow was set to be $U = 12\ m/s$. For a Reynolds number as high as the current, setting the initial velocity too high can lead to stability problems why this value of around half the free-stream velocity was chosen. The initial conditions for the turbulence kinetic energy and dissipation was chosen to be the same as for those quantities at the inlet boundary.

3.3 Numerical Set-Up

To produce a reliable result the time step of the simulation was chosen with the desire that the CFL number, defined in eq. (23), as would stay under 1. The same time step as in Östh and Krajnović [9], $t = 4 \cdot 10^{-5}\ s$ was used for all three mesh sizes. It would be counterproductive using a smaller time step since the purpose of PANS is to alleviate computational effort compared to LES. Instead a larger timestep could have been used for the smaller coarser meshes following the CFL condititon defined in eq. (23).

The three different discretization schemes presented in section 2.6; Central Differencing, AVL Smart, and MINMOD, were all used in different runs to solve the momentum equation. When the Central Differencing scheme was used it was blended with 4% of the Upwind Scheme. The continuity equation was discretized with 100% Central Differencing and the turbulent quantities were discretized using MINMOD.

For the coarse, medium, and fine meshes; 3, 5, and 9 computation nodes were used respectively, resulting in about 100 000 cells/core.

3.4 Results

No satisfactory results were obtained for this case using PANS. After behaving as expected in the initialising part of the simulation, the fluctuations died out as the flow became fully developed. This happened for all three mesh sizes and also for almost all different configurations of boundary condition and differencing schemes. The only case where the fluctuations did not fully die out was when the momentum equations was discretized using central differencing, but even here they were small. This occurrence has never before been presented when using PANS for bluff bodies.

Since the same behaviour is noticed in all cases mainly results from the largest will be presented here and will thus represent the others as well. As it could be determined quite early on that the simulations would turn steady, based on the force signals, most cases were discontinued when this established. Thus meaningful time averaged 3D data were not captured for these cases. However only small difference were observed in the force signals for all cases. These differences were after how long the flow field turns steady and also to what value the forces converge.

The phenomenon is visualized in fig. 5 using the forces acting upon the truck. The drag forces are acting in the x-direction of the domain, the lift forces in the y-direction and the side forces in the z-direction. The fluctuating forces that appear in the early stage stages of the graph is not expected to die out as they do in this case. Instead they are expected to converge to fluctuate around a mean value.

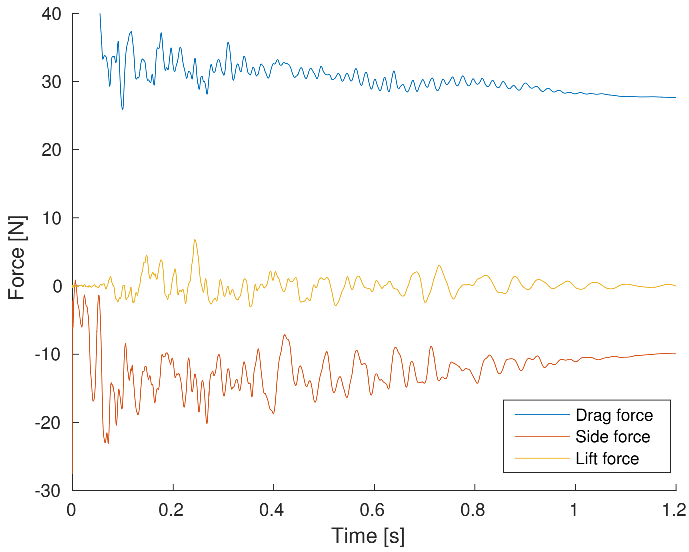

Figure 5: Forces acting on truck as simulated by PANS

In fig. 6 the instantaneous velocity field of the symmetry plane after two flow through passages is visualized and in fig. 7 the time averaged from $t = 0$ to $t = 0.8s$, or roughly two flow through passages, is visualized. It can clearly be seen that these visualizations are close to identical. Of course the instantaneous velocity field is expected to be more stochastic and not be this smoothed out which agrees with the statement that the flow field has turned steady.

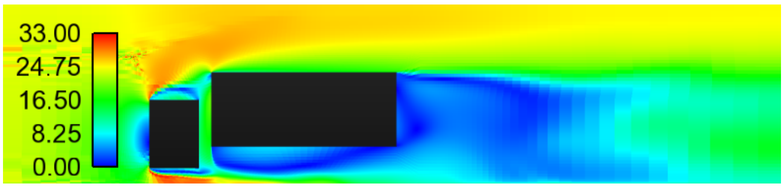

Figure 6: Instantaneous velocity in symmetry plane $[m/s]$

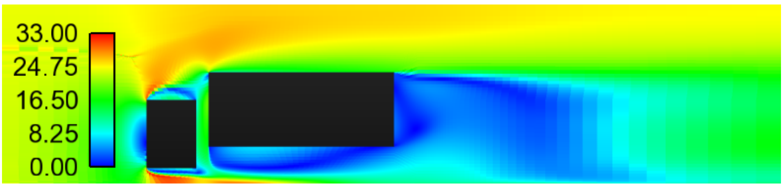

Figure 7: Time averaged velocity in symmetry plane $[m/s]$

3.4.1 Coefficients

As measurements to quantify the simulation the drag coefficient, C_D, and pressure coefficient, C_p were used. Early on in the simulation these coefficients gave somewhat encouraging results only to diverge from the reference LES with time.

$$
\begin{aligned}
C_p &= \frac{P - P_\infty}{0.5 \cdot \rho U_\infty^2} \\
C_D &= \frac{F_{drag}}{0.5 \rho U_\infty b^2}
\end{aligned} \tag{31}
$$

In fig. 8 the measured drag forces that acted upon the truck is compared to the force that would correspond to a drag coefficient of 1.023, which is the one that was found for the fine mesh in Östh and Krajnović [9]. This force was calculated to 34.1105 N. It can be seen that early on in the simulation the measured force comes reasonably close to the reference, but that this force diverges from the reference until the fluctuations die out completely.

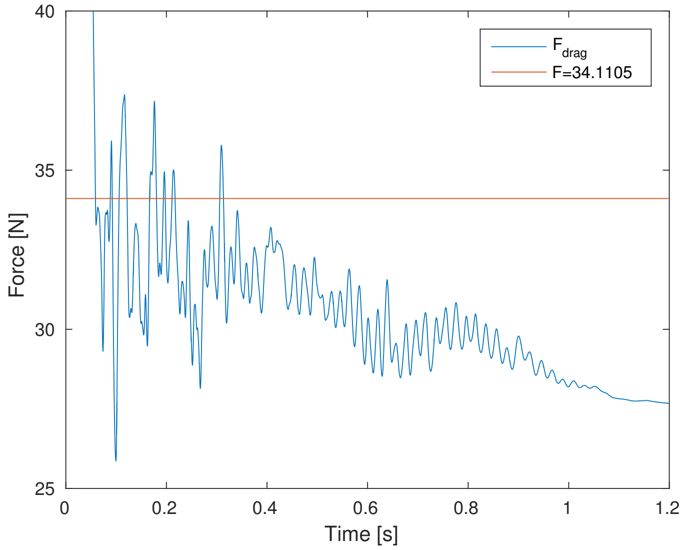

Figure 8: Drag force acting on truck

In fig. 9 the pressure coefficient averaged from $0s$ to $0.495s$ is plotted along the local coordinate η over face box of the truck. The coordinate starts from the origin and continues in the positive y-direction over the front face followed by the top, base and ground faces. The PANS profile for the coarse mesh is here compared to the fine mesh of the reference LES of Östh and Krajnović [9].

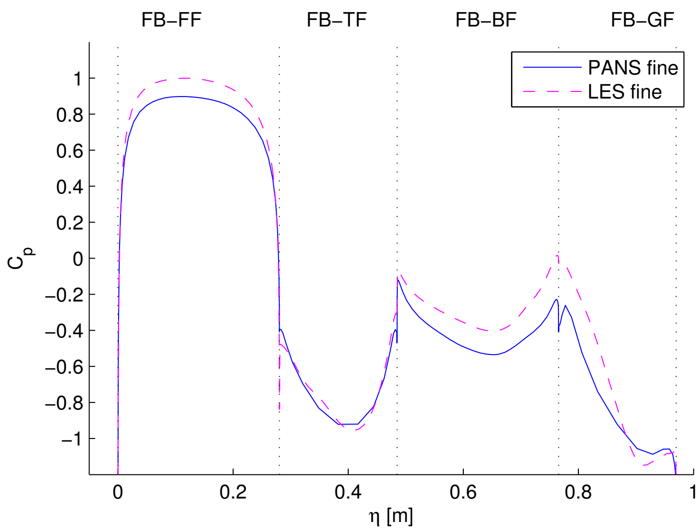

Figure 9: C_p at symmetry plane of front box after one flow passage

Since the pressure coefficient profile for the PANS simulation in fig. 9 is averaged from $t = 0s$ and can obviously not be expected to give an accurate prediction, given that this averaging contains the initialization of the flow. Anyway it can clearly be seen that the profile has similar features to the fully developed and appropriately averaged LES of Östh and Krajnović [9]. Given these results it is deemed possible that a properly averaged PANS solution would converge to good agreement with the reference LES if the simulation had not turned steady.

In fig. 10 the same profiles are plotted, where the coefficient is averaged from $t = 0s$ to $t = 0.822s$. Comparing the two PANS profiles it can be seen that when the coefficient is getting further from the reference LES solution with time, which is to be expected with the fluctuations dying out.

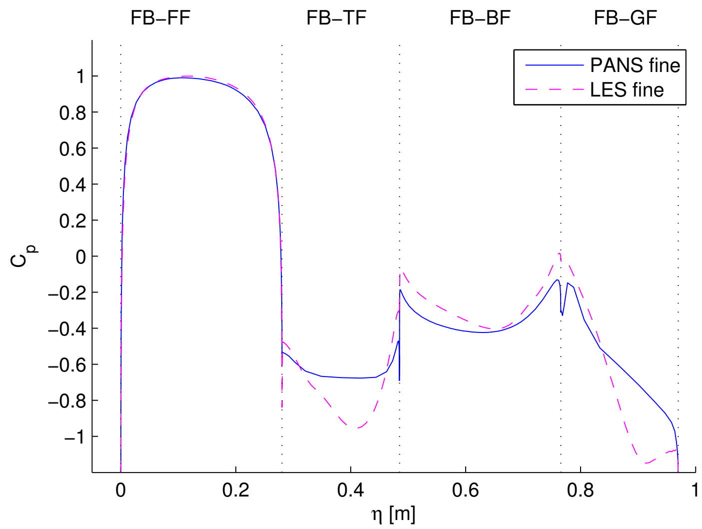

Figure 10: C_p at symmetry plane of front box after two flow passages

The unresolved-to-total-kinetic-energy-ratio, f_k, is visualized in fig. 11 here in the symmetry plane of the domain. Here it can be seen that close to the truck the solution is reduced to RANS. A similar distribution of this ratio is obtained for all configurations and mesh sizes. Ideally f_k should be around 0.3 close to the body to obtain good results.

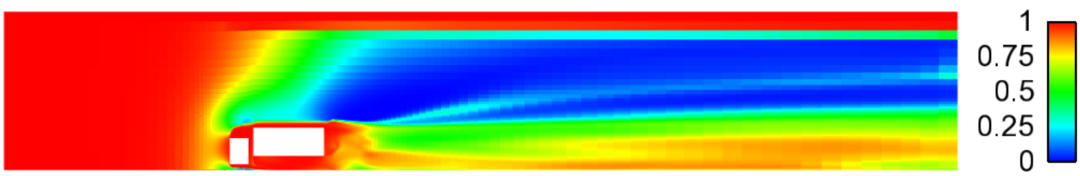

Figure 11: Unresolved-to-total-kinetic-energy-ratio f_k in the symmetry plane

3.4.2 Streamline Patterns

In fig. 12 the time averaged streamlines at the plane $y = 0.46b$ is visualized after one and two flow passages respectively. The time averaging is started at time zero just as in section 3.4.1. The point where the flow reattaches to the trailer for the shorter time averaging agrees well to what is visually presented in Östh and Krajnović [9]. It can be seen that this point of reattachment wanders downstream considerably as the flow is averaged for a longer time, and thus diverge from the reference. The vortices that can be distinguished does not however correspond well to the reference well in either of the visualizations. Just as in section 3.4.1 the velocity is time averaged from time zero which means that the initialization of the flow will have a bad impact on the streamlines.

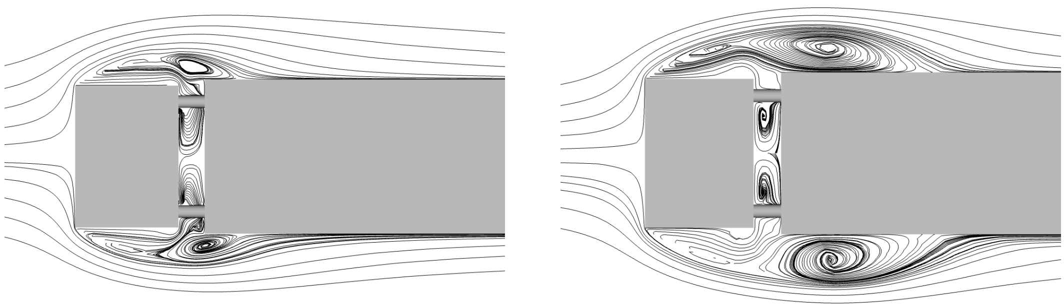

(a) Streamlines at y=0.46b after one flow passage (b) Streamlines at $y = 0.46b$ after two flow passages

Figure 12

In fig. 13 streamline are projected to planes above the front box with the same time averages as in fig. 12. Again the most important thing to note from this illustration is not how the streamlines correspond the what is presented in Östh and Krajnović [9], but how the longer time averaging seem to diverge from the reference LES instead of converging towards it.

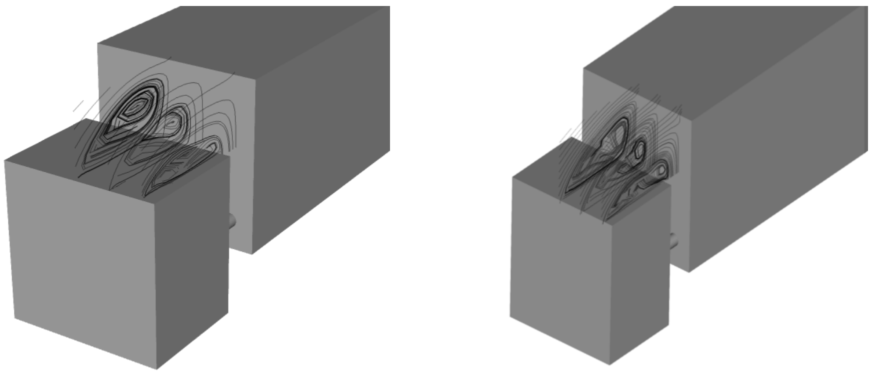

(a) Streamlines above FB after one flow passage (b) Streamlines above FB after two flow passages

Figure 13

3.4.3 Resolution

The non-dimensionalized wall normal unit n^+ for this case is illustrated in fig. 14. It can be seen that in large portions of the surface of the truck the n^+ is actually higher than 1, albeit not by much. However it should be noted that the flow field here is not consistent with the expected unsteady flow.

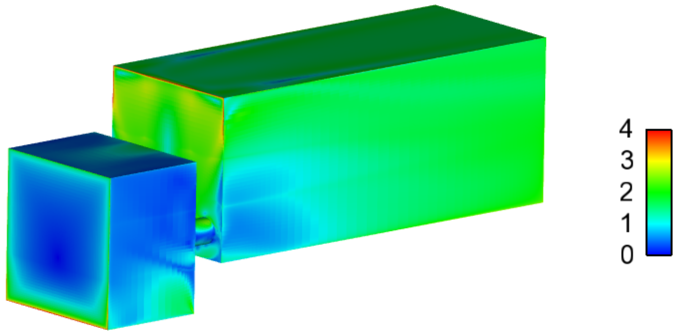

Figure 14: Nondimensionalized wall normal unit n^+

The temporal resolution is visualized in fig. 15 with the CFL-number for the symmtery plane of the domain. It can be seen that the CFL-number stays below one globally. However in small portions of the mesh it is slightly larger. When comparing fig. 15 to fig. 4 it can be seen that these higher values are found in the interfaces of the blocks of the mesh. Similar CFL numbers are found in the rest of the mesh.

Figure 15: CFL-number of symmetry plane

3.5 LES Control Case

As a way to control if the quality and resolution of the mesh might have been insufficient an LES simulation was performed on the medium mesh. This mesh was, as earlier noted, smaller then the coarser mesh used in Östh and Krajnović [9]. All boundary and initial conditions as well as the time step were the same as for the PANS runs. As the behaviour of the simulation more than the actual numerics of the results was of interest here, this run was only carried out for about 3.5 flow passages.

To illustrate the unsteadiness of the simulated flow the forces acting on the truck is presented in fig. 16.

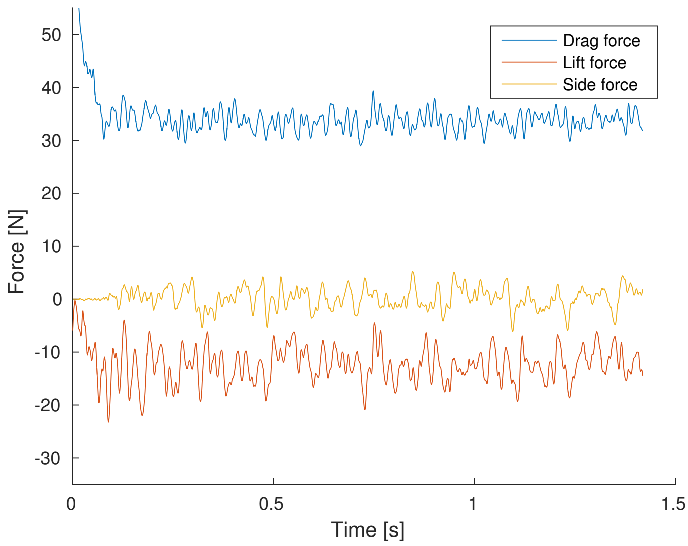

Figure 16: Forces acting on truck as simulated by LES

In table 1, the drag coeffecients of the current LES is presented along with the experimental of Allan [19] and the previous LES of Östh and Krajnović [9]. The drag coefficient of the current LES was averaged from 0.4 s to 1.4192 s

Current LES	Experimental	LES fine	LES coarse
1.0063	1.02	1.023	1.022

Table 1: Drag coefficients

In fig. 17 the pressure coefficient C_p is plotted against the local coordinate η. This coordinate starts in the positive y-direction from the origin and follows the symmetry line of the front box over the surfaces of the four faces back to the origin.

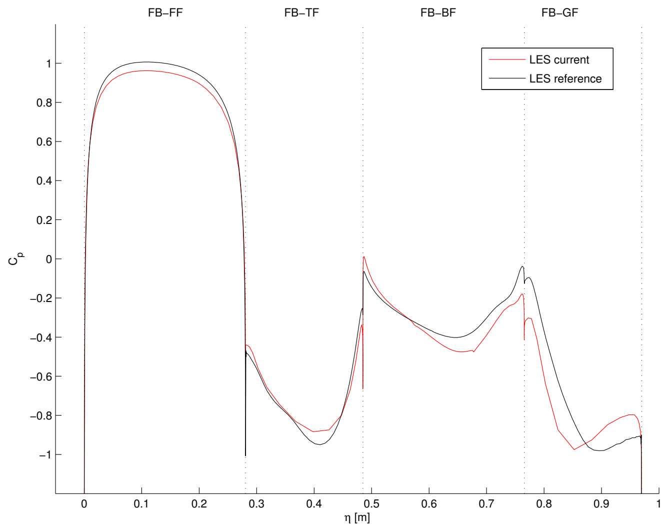

Figure 17: Pressure coefficient along symmetry line of front box

On the basis of these results it can be said that the mesh is sufficiently good to produce LES results in good comparison with the references. Perhaps the more important finding is that the simulations performs as expected in terms of unsteadiness.

3.6 Discussion

The behaviour that the simulation is turning steady is perplexing. Given the bluff body of the truck this is not expected to happen, and both the LES of Östh and Krajnović [9] and section 3.5 of this thesis gives unsteady results. Thus it can with confidence be said that the current PANS simulations are in some way incorrect.

Given that the AVL Fire implementation of PANS has yielded accurate predictions for many bodies, as stated in section 1.1 these results are a one-off. This does suggest that the issue is due some error by the user. From a user perspective the main parameters and settings that can be faulty are; the mesh, the numerics, or turbulent parameters on the inlet boundary.

Since all three built-in numerical schemes were tried to solve the momentum equation, and all converged to give steady solutions, this is clearly not the issue. As stated in section 3.2 two different configurations for the turbulence on the inlet boundary were used and both of these settings resulted in steady solutions as well.

As presented, the wall normal unit, y^+, is a bit higher than ideal, but given the square geometry of the truck this should not be an issue. Nor does the CFL number suggest that the temporal resolution is an issue. Since the LES of section 3.5 gives satisfactory results that would seem to indicate that the quality of mesh is acceptable. Also given the nature of PANS, it should be expected to behave less sensitive to mesh resolution than an LES.

Given that the different settings was exhausted and none of them could produce unsteady results it seems that the issue might not be on the user end any way. It is interesting to note however that the results initially seem to be approaching a good results. Therefore it is deemed likely that if the simulation had not turned steady PANS would have have produced results in good comparison with the references. Thus the main finding of this part of the thesis is this phenomenon of the simulation turning steady. To be able to trust PANS as a turbulence model this cannot happen and that's why this needs further investigation.

As noted the main focus went to analyzing the simulations steady, why much focus was not put to compare differences in results due to different configurations. In hindsight the results for all different configurations of meshes, numerical schemes, and inlet boundary conditions should have been run for a longer time and proper time averages should have been made. The reasoning behind not running all these cases for longer what that the results at the time seemed to be due to some faulty user setting and that more realistic results would be obtained when the issue was resolved. Also part of the reasoning was that computational time and cores were limited. However if these results were available comparisons between these different cases might help to give some lead on the reason to the phenomenon of turning steady. Since the simulation reduces to a RANS solution for all mesh sizes, it would not however be of much interest to compare the solutions of the different mesh sizes with respect to grid independence since the all should be more than sufficient for RANS.

4 Detailed Truck

The fully detailed truck, visualized in fig. 18, is a VOLVO AB truck in half scale. This truck was tested in the 9 m wind tunnel at the National Research Council in Ottawa, Canada. A geometry of the truck along with geometry of the tunnel were provided by VOLVO AB for this project. A cut view of the tunnel is visualized here in fig. 19. The wind tunnel testing was performed with a velocity of $50m/s$. This corresponds to $25m/s$, or $90km/h$, for the full scale truck. A characteristic length for the half scale truck is the height of the trailer which is $1.3m$. This gives a Reynolds number of 4 500 000 based on the height of the trailer.

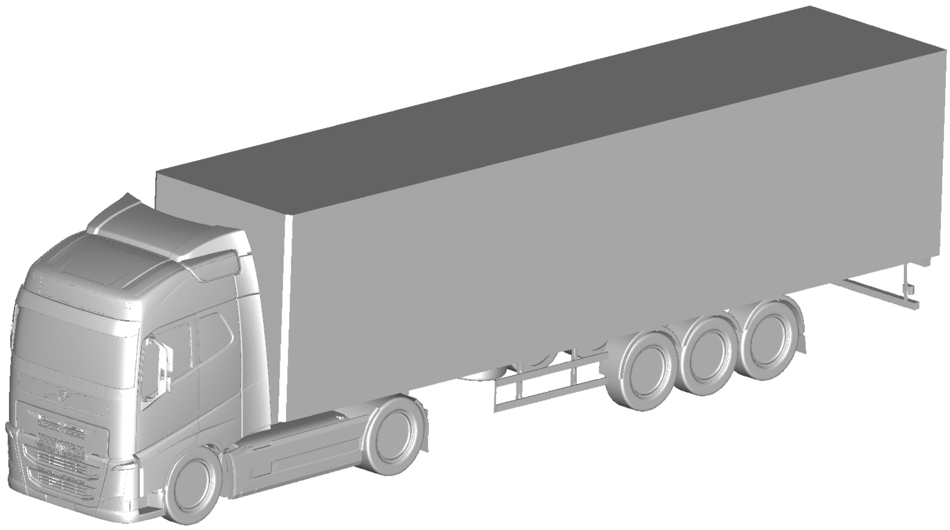

Figure 18: Fully detailed VOLVO truck

4.1 Computational Mesh

The mesh provided by VOLVO AB was not compatible with AVL FIRE. Based on the provided geometry a hexahedral mesh was created with assistance by engineers at AVL, using the AVL Fire automatic mesher *FAME Hexa*.

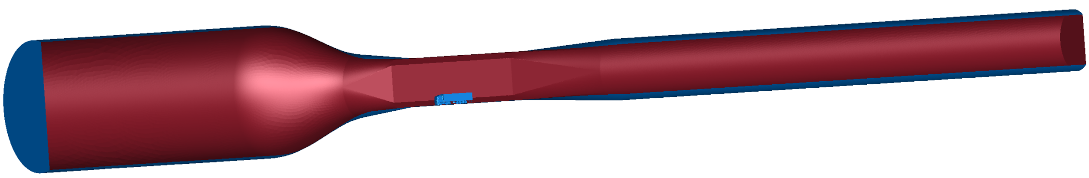

Figure 19: Geometry of exterior of wind tunnel

This mesh consisted of about 150 million cells. One refinement box was placed around the truck and another box for the wake behind the truck. A separate volume was created for the cooling package and was connected to the mesh via an arbitrary interface.

4.2 Boundary Conditions

The boundary conditions of the computational domain were provided by VOLVO AB. These conditions were chosen to mimic the physical wind tunnel set up as accurately as possible.

The velocity of the air at the inlet of the tunnel was $8.213407 m/s$. As the flow passes through the nozzle part of the tunnel it is then accelerated to the test velocity $50 m/s$. A turbulence intensity of 0.3% was set at the inlet, resulting in a turbulence kinetic energy of $4 \cdot 10^{-4} m^2/s^2$ as well as a dissipation rate of $1 \cdot 10^{-3} m^2/s^3$. The outlet was set as a pressure outlet with $0 Pa$.

The entry as well as the exit portions of the tunnel, visualized in fig. 20 as the orange and green parts respectively, were set as slip-walls. The walls of the test section, yellow in fig. 20, were set as no-slip walls with two exceptions. The green part of the floor in fig. 21 is supposed to represent the boundary layer suction area from the real tunnel. To model this suctions area the wall was set as a slip wall. The other exception is the moving floor, magenta in fig. 21. This was set as a moving wall no-slip boundary with a velocity of $50 m/s$ in the positive x-direction.

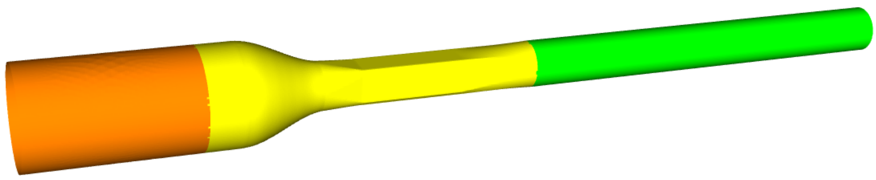

Figure 20: Outer walls of tunnel

The boundary condition at the truck itself, turquoise in fig. 21, was set as a stationary no-slip wall condition, with the exception of the wheels of the tractor part of the truck. Here the boundary conditions of both sets of wheels, blue and red in fig. 20 were set as moving no-slip walls. By specifying a rotational speed, a point on the axis of rotation, as well as the components of the axis of rotation, the velocity components wre calculated by a built-in function in AVL Fire. The rotational speed of the wheels was $181.8182 rad/s$

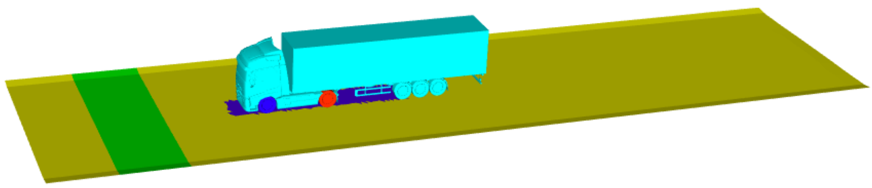

Figure 21: Boundary conditions on truck and test section

4.3 Numerical Set-Up

The momentum equation was solved with the AVL SMART scheme, whereas continutiy equtaion with Central Differencing and the Turbulence equations with MINMOD. Initially a timestep of $5 \cdot 10^{-6}$ s was. A value which later one would have likely been adjusted to obtain a good CFL number.

4.3.1 Cooling Package

The cooling package of the truck is situated right behind the grill. Since it was supposed to be modeled as a porous box it was meshed as a separate volume. This volume had a local coordinate system since it is a little bit rotated around the z-axis. The local coordinate axes are defined with the global coordinates in table 2.

	X_{global}	Y_{global}	Z_{global}
X_{local}	0.9973968153997016	-0.07210820085408828	0
Y_{local}	0.07210820085408828	0.9973968153997016	0
Z_{local}	0	0	1

Table 2: Local coordinate system of Cooling Package

Here it was modeled as a box of porous media using eq. (30). The porosity model used by VOLVO is on the form

$$P = P_v + P_i \cdot |w| \qquad [kg/(m^3 s)] \tag{32}$$

This equation was then multiplied by the velocity to get it on the Darcy-Forchheimer form. The Darcy-Forchheimer coefficients were then expressed through the viscous resistance coefficient P_v and the inertial resistance coefficient P_i as follows

$$\begin{aligned} \alpha &= \frac{P_v}{\mu} \\ \zeta &= \frac{2P_i}{\rho} \end{aligned} \tag{33}$$

The resistance in the local y- and z-directions was a thousand times higher than that in the stream wise x-direction so that the flow would be properly directed. The values provided by VOLVO as well as the converted values are presented in table 3.

Coordinate	P_v $[kg/m^4]$	α $[1/m^2]$	P_i $[kg/(m^3s)]$	ζ $[1/m]$
X_{local}	294.75	159.67	41.1	68.27
Y_{local}	29475	15967	4110	6827
Z_{local}	29475	15967	4110	6827

Table 3: Values for porous modeling of cooling package in local coordinates

These values were then transformed to correspond to the global coordinate system via a linear interpolation. Since the rotation was around the z-axis, the resistances in the z-direction will remain unchanged.

Coordinate	α $[1/m^2]$	ζ $[1/m]$
X_{global}	726.2738	310.5324
Y_{global}	15081	6448.2
Z_{global}	15967	6827

Table 4: Values for porous modeling of cooling package in global coordinates

4.4 Computational Difficulties

Some computational problems were found when trying to simulate the case. Firstly it was found that the 2014 version of the AVL FIRE 2014 [18] solver could not save 3D data for post-processing in Ensight 10.0.1 [21]. The case would run as expected until it was prompted to save 3D data and then the simulation would crash. In the 2014.2 version of the simulation would not start at all. When using the 2016 version of the solver 3D data could be saved.

The other difficulty was trying to save backup and restart files. These files are necessary to not have to start over from time zero whenever the allocated time on the computation nodes runs out, or the simulation stops or crashes for some other reason. Since it's hard to appreciate how much time that should be allocated for each simulation, these files are quite crucial to be able to get good results. When computing on the thin computational nodes, the simulation crashed whenever it was prompted to write backup or restart files, no matter which version of the solver that was used. It did not help however many or few nodes that were used. If the simulation instead was run on fat nodes these backup files could be written. However, as noted insection 2.8, given the limited amount of fat nodes, this fact severely restricted the possibility to perform simulations in a timely manner.

Other ways to come around this issue could be to run on fewer cores per node but instead increase the number of nodes. This would however increase the computational cost of the simulation as more nodes would be used. It might also be solved by using a smaller number of fat nodes alongside with the thinner nodes. Then the saving of the files would have to be done by the fat nodes.

4.5 Results and Discussion

Given the difficulties presented in section 4.4 no meaningful results due to the limited time frame for this project and also limited computing recources. It does seem the simulation running out of memory when saving backup files might be a reasonable explanation for the crashes. However this does not explain the seemingly random crash that was experienced once. At the very least these results can act as a reference if similar results are experienced in the future.

If more time was given for this project the first step would be to get this simulation to run without crashes. Once this could be solved the simulation would have been run for a sufficient period of time to be able to analyze the resolution of the mesh and then eventually make some necessary adjustments. Given a mesh with good resolution a fully time-averaged solution should have been produced and thus compared to test data obtained by AB VOLVO. The next step would then be to evaluate if results were produced in a time and to a computational cost that could be motivated in the industry by the quality of the results.

5 Instability of Notchback Ahmed Body Wake

The Ahmed Body is a well documented generic body, first presented in Ahmed, Ramm, and Faltin [22], that has features resembling a car. In Sims-Williams, Marwood, and Sprot [10] the rear end geometry of a notchback version of such bodies is studied, and more specifically the effect of different effective backlight angles on the flow field. Such a body is vizualised in fig. 22 and in fig. 23 a visual definition of the backlight angle B_{eff} can be seen. Sims-Williams, Marwood, and Sprot [10] studied different geometries using both wind tunnel measurements and CFD, at a Reynolds number of $1.9 \cdot 10^6$ based on the length of the model. The findings include that for certain effective backlight angles an asymmetric wake flow features arises even though the boundary conditions, body, and mesh are all symmetric. This asymmetry phenomenon is only found when the separated flow on the backlight reattaches before the end of the trunk. For an in depth analysis of this the reader is referred to this paper.

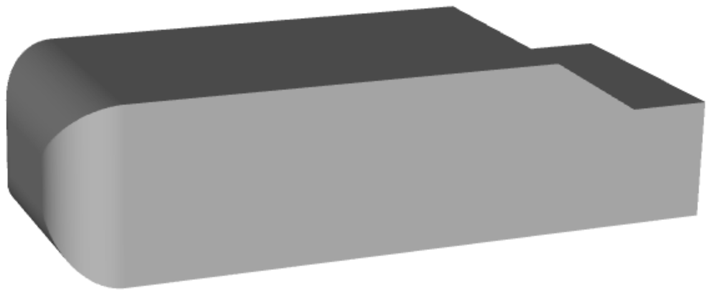

Figure 22: Notchback Ahmed Body

For the case with an effective backlight angle of $B_{eff} = 17.8^o$ and $B = 31.8^o$ it is found that a clear asymmetry of the wake can be observed. This asymmetry can be seen to start in the separation of the flow on the notchback itself and further continue in the wake. In this section of the thesis PANS will be used to try to reproduce these results. In the current simulations a smaller model, with model length $0.36667m$, was used which was then compensated for with a higher simulated velocity.

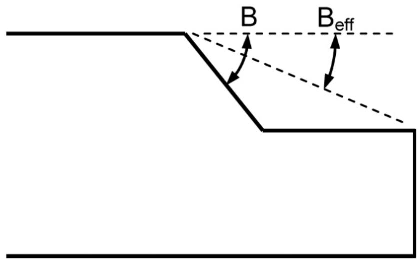

Figure 23: Definition of backlight angle (figure from Sims-Williams, Marwood, and Sprot [10])

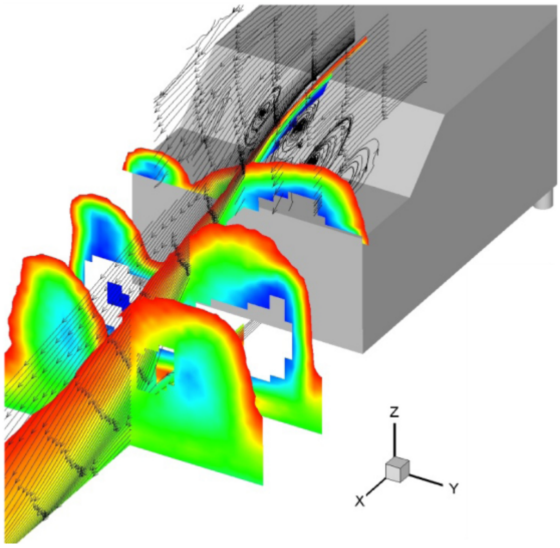

Figure 24: Asymmetry in wake of Ahmed body (figure from Sims-Williams, Marwood, and Sprot [10])

In fig. 24 the asymmetry of this case is visualized. From the streamlines on the backlight a clear asymmetry can be seen in the vorticial structure. On the right side of the symmetry plane the streamlines indicates a vortex, whereas on the opposite side this vortex disappears. Also in the three planes that are colored by the pressure coefficient an asymmetry can be distinguished.

5.1 Computational Mesh

The mesh was for this was made in ANSYS ICEM CFD 14.0 [20] and consisted of almost 27 000 000 cells. The domain of this simulation can be seen in fig. 25

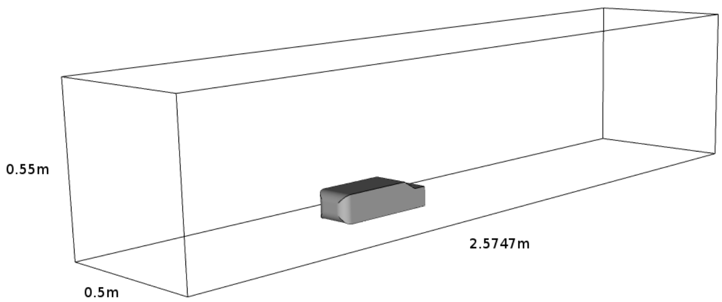

Figure 25: Computational Domain

5.2 Boundary & Initial Conditions

The inlet boundary condition for the domain was set as a uniform velocity of $78.2285 m/s$ with a prescribed turbulence kinetic energy $k = 0.0764962 m^2/s^2$ and dissipation rate $156.386 m^2/s^3$. The turbulence quantities were calculated according to section 2.4 and corresponds to a turbulence intensity of $0.005 = 0.5\%$. The homogeneous Neumann boundary condition was used for the outlet of the domain.

A moving wall boundary condition was used at the floor of the domain to stop a boundary layer building up at the floor and thus mimic real life road conditions better. This velocity was the same as the inlet velocity, $78.2285 m/s$. The remaining walls as well as the body itself was set as no-slip walls.

The domain was initialised at a lower velocity, $40 m/s$, than the test velocity. This was done to acheive stability of the solution, but also not have to start from a stagnant flow and thus take a longer time to reach a fully developed flow. The turbulence quantities were set very close to the inlet quantities.

5.3 Numerical Set-Up

The simulation was run on 21 nodes corresponding to 192 cores. This results in about 89 000 nodes/core. The numerical schemes were chosen based on experience in the research group. To solve the momentum equation AVL SMART differencing scheme was used. For the continuity equation central differencing was used and for the turbulence equations the MINMOD scheme was used. A time step of $1 \cdot 10^{-6}$ was used.

5.4 Results

The simulation was considered fully developed after, about $0.063 s$ corresponding to roughly two flow through passages of the domain. After this the time averaging of the flow was started but was only time averaged for roughly just over one flow passage. This short averaging was due to time limitations of the project.

When looking at the unresolved-to-total-kinetic-energy-ratio f_k in fig. 26 it can be seen that the values are generally in a good range for PANS, which is somewhere in the range $0.3 - 0.5$.

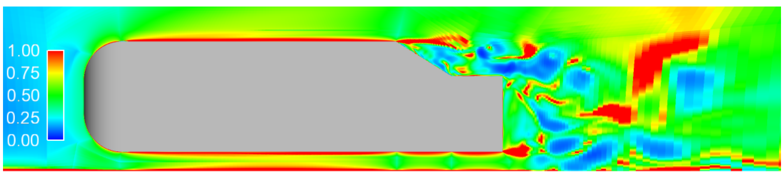

Figure 26: Unresolved-to-total-kinetic-energy-ratio f_k around body

5.4.1 Resolution

The temporal resolution characterized in fig. 27 by the CFL number, can be seen to be well below the desired value of 1 globally. The spatial resolution is visualized in fig. 28. Also the y^+ is generally under 1 globally and is considered acceptable.

Figure 27: CFL number of symmetry plane

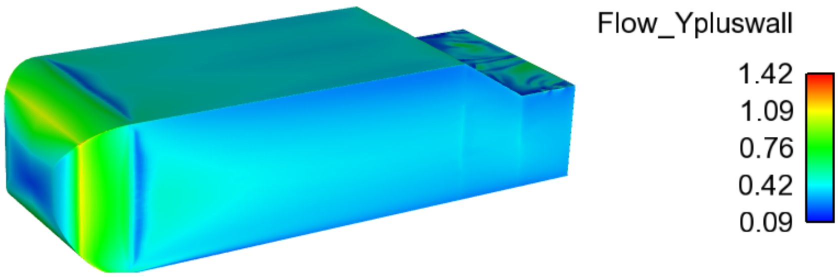

Figure 28: y^+ of Ahmed Body

5.4.2 Asymmetry

In fig. 29 it can be seen that the flow that has separated on the backlight of the body has not been reattached before the end of the trunk. Given what was found in Sims-Williams, Marwood, and Sprot [10] this indicates that there will not be any asymmetry of the flow field.

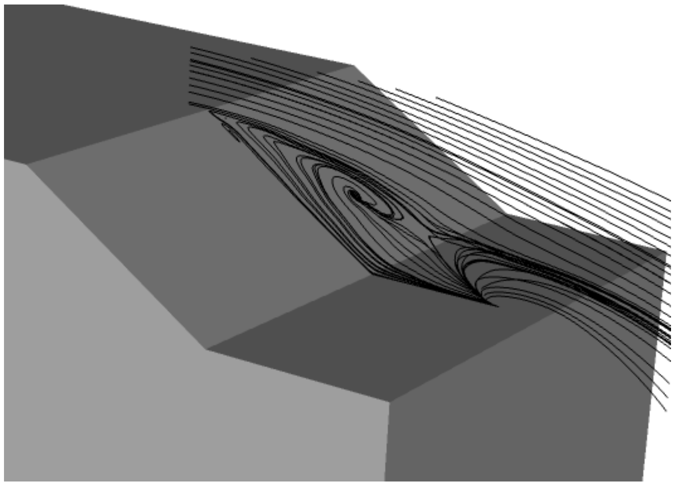

Figure 29: Time averaged streamlines at symmetry plane of trunk

To give some understanding of the flow field on the backlight the stream lines of five different planes are visualized in fig. 30. These planes are $\frac{y}{\sqrt{A}} = 0$, $\frac{y}{\sqrt{A}} = \pm 0.00334711$, and $\frac{y}{\sqrt{A}} = \pm 0.00669421$. The visualized streamline patterns seems to be symmetrical with regards to the symmetry plane. At all planes except the symmetry plane the flow seems to be reattaching.

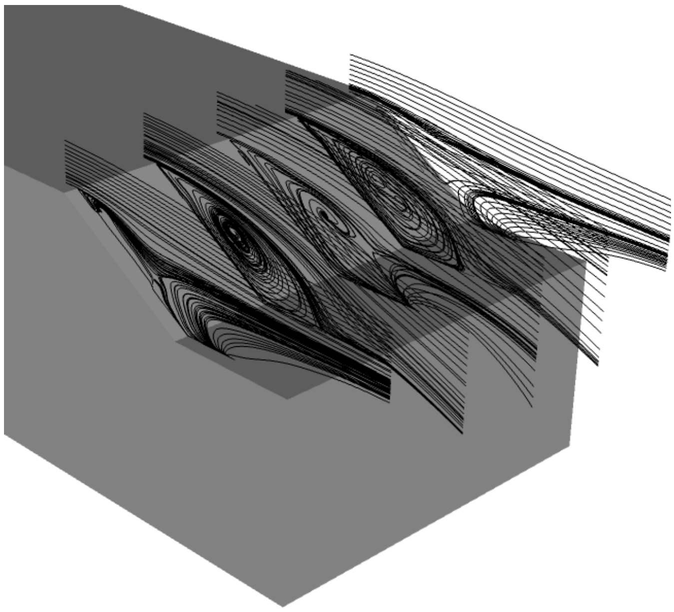

Figure 30: Time averaged streamlines on backlight at five different planes

When analyzing the symmetry of the wake the pressure coefficient is used; $C_p = \frac{P-P_\infty}{0.5 \cdot \rho \cdot U_\infty}$. The pressure coefficient of three different planes in the wake of the boduy is visualized in fig. 31.

From these figures no asymmetry can be observed either.

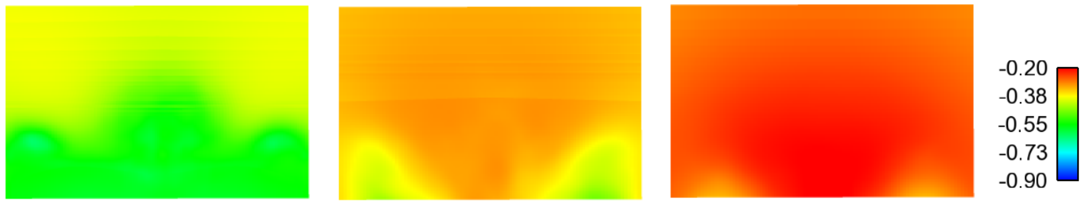

(a) C_p at $x/\sqrt{A} = 0.03$ (b) C_p at $x/\sqrt{A} = 0.5$ (c) C_p at $x/\sqrt{A} = 1.0$

Figure 31

The placement of these planes can be seen in fig. 32

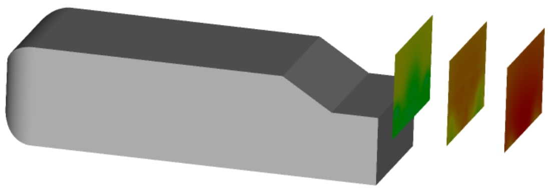

Figure 32: Placement of planes in wake

5.5 Discussion

It should be noted that the time that the flow was averaged for is clearly insufficient, but given the time available this could not be helped. An obvious suggestion for future works would be firstly to let the flow developed for a longer time, and more importantly; to make a proper time averaging of the flow. Since the time was so short it cannot be said with confidence that an asymmetry won't be developed. However given the results that was obtained there are no indications that any asymmetry exists.

Given the resolution of the simulation the mesh and time step should be good enough to produce accurate results. Also the f_k factor suggests a good PANS solution. These both facts suggests that the simulation in itself is good.

Since the data suggests that the simulation is valid, a possibility that should be entertained is that the prediction of the current simulation is accurate and that the asymmetry might not exist. Another possibility could be that the asymmetry might take a comparably long time to develop. Given that the reference results come from experiments, long periods of time can be studied. For a PANS simulation at the current Reynolds number only fractions of a second can be simulated. Thus a speculation is that the PANS simulation might not be able to capture the asymmetry.

6 Conclusion

Given the results of the three different cases that were run, it can not be said that that the aims of this thesis were reached. However this does not mean that the findings are not of interest. Generally this thesis can give insight to problems and difficulties a user of the PANS model and the AVL Fire solver might run in to for certain simulations.

For the generic truck in section 3 the main finding was that the simulation did not produce time dependent results as should be expected by PANS. Since PANS is an unsteady turbulence model these are results that should not be obtained when using the model in industry. Since there is no documentation of a PANS simulation turning steady before it could be seen as an anomaly. To be able to fully trust the model the reason for this occurrence should nevertheless be thoroughly examined.

Since no simulations could be run for the fully detailed truck in section 4, no conclusions could be drawn here regarding the PANS implementation in AVL Fire. Instead the focus lies on the difficulties that restricted the possibility of obtaining meaningful results. Some investigation and development regarding the memory handling problems when saving data for large industrial cases such as this one could result in a much more user-friendly solver.

For the Ahmed body case in section 5 the current simulation suggests that no asymmetry is found for the body at this Reynolds number. However as the results of the reference indicates otherwise the PANS simulations should be studied further and more specifically simulated for a longer physical time.

References

[1] T Kobayashi and M Tsubokura. "CFD application in automotive industry". In: *100 Volumes of 'Notes on Numerical Fluid Mechanics'* (2009), pp. 285–295.

[2] Charles G Speziale. "Computing non-equilibrium turbulent flows with time-dependent RANS and VLES". In: *Fifteenth International Conference on Numerical Methods in Fluid Dynamics*. Springer. 1997, pp. 123–129.

[3] PR Spalart, WH Jou, M Strelets, SR Allmaras, et al. "Comments on the feasibility of LES for wings, and on a hybrid RANS/LES approach". In: *Advances in DNS/LES* 1 (1997), pp. 4–8.

[4] Bruno Chaouat and Roland Schiestel. "A new partially integrated transport model for subgrid-scale stresses and dissipation rate for turbulent developing flows". In: *Physics of Fluids (1994-present)* 17.6 (2005), p. 065106.

[5] Sharath S Girimaji, Ravi Srinivasan, and Euhwan Jeong. "PANS turbulence model for seamless transition between RANS and LES: fixed-point analysis and preliminary results". In: *ASME/JSME 2003 4th Joint Fluids Summer Engineering Conference*. American Society of Mechanical Engineers. 2003, pp. 1901–1909.

[6] Branislav Basara, Siniša Krajnovic, Sharath Girimaji, and Zoran Pavlovic. "Near-wall formulation of the partially averaged Navier Stokes turbulence model". In: *AIAA journal* 49.12 (2011), pp. 2627–2636.

[7] Chi-Su Song and Seung-O Park. "Numerical simulation of flow past a square cylinder using partially-averaged Navier–Stokes model". In: *Journal of Wind Engineering and Industrial Aerodynamics* 97.1 (2009), pp. 37–47.

[8] Maryam Mirzaei, Siniša Krajnović, and Branislav Basara. "Partially-Averaged Navier–Stokes simulations of flows around two different Ahmed bodies". In: *Computers & Fluids* 117 (2015), pp. 273–286.

[9] Jan Österh and Siniša Krajnović. "The flow around a simplified tractor-trailer model studied by large eddy simulation". In: *Journal of Wind Engineering and Industrial Aerodynamics* 102 (2012), pp. 36–47.

[10] DB Sims-Williams, David Marwood, and AJ Sprot. "Links between notchback geometry, aerodynamic drag, flow asymmetry and unsteady wake structure." In: *SAE International journal of passenger cars. Mechanical systems.* 4.1 (2011), pp. 156–165.

[11] Sharath S Girimaji. "Partially-averaged Navier-Stokes model for turbulence: A Reynolds-averaged Navier-Stokes to direct numerical simulation bridging method". In: *Journal of Applied Mechanics* 73.3 (2006), pp. 413–421.

[12] M Germano. "Turbulence: the filtering approach". In: *Journal of Fluid Mechanics* 238 (1992), pp. 325–336.

[13] Sharath S Girimaji and Khaled S Abdol-Hamid. "Partially averaged Navier–Stokes model for turbulence: implementation and validation". In: *AIAA paper* 502 (2005), p. 2005.

[14] K Hanjalić, M Popovac, and M Hadžiabdić. "A robust near-wall elliptic-relaxation eddy-viscosity turbulence model for CFD". In: *International Journal of Heat and Fluid Flow* 25.6 (2004), pp. 1047–1051.

[15] M Popovac and K Hanjalic. "Compound wall treatment for RANS computation of complex turbulent flows and heat transfer". In: *Flow, turbulence and combustion* 78.2 (2007), pp. 177–202.

[16] Henk Kaarle Versteeg and Weeratunge Malalasekera. *An introduction to computational fluid dynamics: the finite volume method*. Pearson Education, 2007.

[17] Peter K Sweby. "High resolution schemes using flux limiters for hyperbolic conservation laws". In: *SIAM journal on numerical analysis* 21.5 (1984), pp. 995–1011.

[18] AVL List GmbH. *AVL FIRE 2014*. 2014. URL: `https://www.avl.com/fire2`.

[19] JW Allan. "Aerodynamic drag and pressure measurements on a simplified tractor-trailer model". In: *Journal of Wind Engineering and Industrial Aerodynamics* 9.1-2 (1981), pp. 125–136.

[20] ANSYS. *ANSYS ICEM CFD 14.0*. 2011. URL: `http://resource.ansys.com/Products/Other+Products/ANSYS+ICEM+CFD`.

[21] CEI Software. *Ensight 10.0.1*. 2012. URL: `https://www.ensight.com/`.

[22] SR Ahmed, G Ramm, and G Faltin. *Some salient features of the time-averaged ground vehicle wake*. Tech. rep. SAE Technical Paper, 1984.